PNAS RESEARCH ARTICLE | BIOPHYSICS AND COMPUTATIONAL BIOLOGY

Spatiotemporally mapping temperature dynamics of lysosomes and mitochondria using cascade organelle-targeting upconversion nanoparticles

Xiangjun Di[a,1], Dejiang Wang[a,1], Qian Peter Su[b,2], Yongtao Liu[a], Jiayan Liao[a], Mahnaz Maddahfar[a], Jiajia Zhou[a], and Dayong Jin[a,c]

Edited by David Weitz, Harvard University, Cambridge, MA; received April 28, 2022; accepted October 13, 2022

The intracellular metabolism of organelles, like lysosomes and mitochondria, is highly coordinated spatiotemporally and functionally. The activities of lysosomal enzymes significantly rely on the cytoplasmic temperature, and heat is constantly released by mitochondria as the byproduct of adenosine triphosphate (ATP) generation during active metabolism. Here, we developed temperature-sensitive LysoDots and MitoDots to monitor the in situ thermal dynamics of lysosomes and mitochondria. The design is based on upconversion nanoparticles (UCNPs) with high-density surface modifications to achieve the exceptionally high sensitivity of 2.7% K^{-1} and low uncertainty of 0.8 K for nanothermometry to be used in living cells. We show the measurement is independent of the ion concentrations and pH values. With Ca^{2+} ion shock, the temperatures of both lysosomes and mitochondria increased by ∼2 to 4 °C. Intriguingly, with chloroquine (CQ) treatment, the lysosomal temperature was observed to decrease by up to ∼3 °C, while mitochondria remained relatively stable. Lastly, with oxidative phosphorylation inhibitor treatment, we observed an ∼3 to 7 °C temperature increase and a thermal transition from mitochondria to lysosomes. These observations indicate different metabolic pathways and thermal transitions between lysosomes and mitochondria inside HeLa cells. The nanothermometry probes provide a powerful tool for multimodality functional imaging of subcellular organelles and interactions with high spatial, temporal, and thermal dynamics resolutions.

lysosome | mitochondria | nanothermometry | upconversion nanoparticles (UCNPs)

Significance

The temperature dynamics inside living cells play a critical role in maintaining the cells' homeostasis or driving the cells into dysfunction status. Here, we developed temperature-sensitive LysoDots and MitoDots to monitor the in situ temperature dynamics with specific organelle-targeting strategies. We demonstrated both LysoDots and MitoDots for simultaneously mapping the in situ lysosomal and mitochondrial thermal dynamics and thermal transitions in living cells with high sensitivity. Our observations indicate different metabolic pathways and thermal transitions between lysosomes and mitochondria. The nanothermometry probes provide a powerful tool for multimodality functional imaging of subcellular organelles and interactions with high spatial, temporal, and thermal dynamics resolutions.

Intracellular temperature and its dynamics are vital to maintaining the homeostasis of organelles as well as their biochemical reactions and metabolic processes. Thermal variations indicate whether cells are under healthy physiological or disease status (1, 2). The coordination of different organelles is required to maintain intracellular homeostasis and normal cellular functions. The intracellular organelles not only possess their specific functions but also communicate with each other through membrane contacts or membrane fusion, which together contribute to the survival, growth, and division of the cells. Lysosomes and mitochondria, as the two major contributors to enzyme activity and energy production, are essential to cellular metabolism, participating in many key biological processes such as autophagy, proliferation, cell death (3, 4), etc. Dysfunction of lysosomes and mitochondria has been found in several diseases (5).

The maintenance of both lysosomal and mitochondrial physiological functions and cellular homeostasis relies on intracellular temperature dynamics (6, 7). Lysosomes are highly dynamic organelles responsible for the turnover of some proteins and lipids through digestive enzymes (8). The enzymatic activities are highly dependent on a healthy pH and temperature environment. During the process of heatstroke, the pH values of lysosomes have been observed to increase, which leads to cell death. A higher or lower temperature may reduce enzymatic activities and further disturb cellular homeostasis (9). Mitochondria are involved in cellular respiration and function as the energy factory (10). During the respiratory activity, mitochondria transform energy from carbohydrates to adenosine triphosphate (ATP), simultaneously releasing heat as a byproduct.

Due to the lack of enabling techniques and tools, the functions of lysosomes and mitochondria have been independently studied in the past, though there must be intense cross-talk between the two organelles (3): Dysfunctional mitochondria lead to the elevation of lysosomal pH (11); and in some lysosomal storage diseases, the defects in the lysosomes also contribute to the dysfunction of mitochondria because the abnormal mitochondria cannot be cleared by lysosomes, leading to pathological signaling (12). At present, the interactions of lysosomes and mitochondria are usually studied from either their direct physical membrane contacts using superresolution microscopy (13) or

Author contributions: X.D., Q.P.S., and D.J. designed research; X.D., D.W., Q.P.S., Y.L., and J.L. performed research; X.D., D.W., Q.P.S., and M.M. contributed new reagents/analytic tools; X.D., D.W., and Q.P.S. analyzed data; and X.D., Q.P.S., J.Z., and D.J. wrote the paper.

The authors declare no competing interest.

This article is a PNAS Direct Submission.

[1]X.D. and D.W. contributed equally to this work.

[2]To whom correspondence may be addressed. Email: qian.su@uts.edu.au.

This article contains supporting information online at http://www.pnas.org/lookup/suppl/doi:10.1073/pnas.2207402119/-/DCSupplemental.

Published November 2, 2022.

signaling pathways using molecular biology tools (3). It is unclear how the spatiotemporal thermal dynamics of lysosomes and mitochondria contribute to maintaining homeostasis during pathological processes within a living cell.

Up to now, a series of nanothermometers based on fluorescence or luminescence imaging have been reported, including small organic dyes (14, 15), green fluorescent proteins (GFPs) (16, 17), polymeric nanoparticles (18), nanodiamonds (19, 20), quantum dots (21), and lanthanide-doped nanoparticles (22, 23). The applications of intracellular thermometry in living cells have uncovered spontaneous thermogenesis and temperature variation (24–26). Rationally designed luminescent Ln^{3+}-bearing polymeric micellar probes (Ln = Sm, Eu) have been used to measure the thermogenesis in individual cells, revealing the inhomogeneous intracellular temperature progressions (27). Moreover, lysosome-targeting luminescent lanthanide complexes have been developed to simultaneously image the pH and temperature in the lysosomes (28, 29). Additionally, several thermometers have been proposed for in vivo temperature sensing. For example, Ag_2S nanodots have been used to monitor brain thermoregulation (30) and lanthanide-doped upconversion nanoparticles (UCNPs) have been used for subcutaneous thermal sensing (22). The unique photophysical properties, such as high brightness, superior photochemical stability, excellent temperature-responsive optical properties with large anti-Stokes shifts and long luminescence lifetimes, make UCNPs favorable to temperature sensing (31). Though many advances have been made in using UCNP-based nanothermometers to monitor the temperature variations in living cells, tissues, or animals (32, 33), organelle-specific temperature sensing remains challenging in the physiological environment.

Here, we report surface modifications of high-density polymer linkers that can assist UCNPs to be specifically guided and accumulated into lysosomes and mitochondria in living cells. We established a cascade-targeting strategy in this work. We first introduce $PEGMEMA_{80}$-*b*-$EGMP_3$ di-block copolymers to transfer the hydrophobic UCNPs to hydrophilic ones that can be internalized through the endocytosis process and ended in the lysosomes (34). We name the structure of UCNPs@copolymer as LysoDots. To facilitate the escape of UCNPs from lysosomes and relocation to pass through the potential barrier of the mitochondrial membrane, we then introduce Poly-L-lysine (PLL) to further functionalize UCNPs with a mitochondrial targeting moiety with high lipophilicity, (3-carboxypropyl)triphenylphosphonium bromide (TPP) (34). We then name the structure of UCNPs@PLL@TPP as MitoDots. This strategy allows two sets of nanothermometers with organelle-targeted properties to simultaneously and quantitatively sense the in situ temperature dynamics of lysosomes and mitochondria. The series of LysoDots and MitoDots demonstrate a relative temperature sensitivity at 32 °C of 2.7% K^{-1} and a temperature uncertainty of 0.8 K in HeLa cells, and more importantly, their performances are independent of the ion concentrations or pH conditions. We have observed intriguing spatiotemporal temperature dynamics in HeLa cells: 1) with organelle nonspecific Ca^{2+} ion shock, both lysosomal and mitochondrial temperatures increase 2 to 4 °C; 2) with lysosome-specific drug treatment, the lysosomal temperature drops ∼3 °C while the mitochondrial temperature remains 37 °C; 3) with mitochondria-specific drug treatment, we observed an interesting temperature increment (3 to 7 °C) and spatiotemporal thermal transition (1- to 2-min delay) from mitochondria to lysosomes. These observations indicate different metabolic pathways and thermal transitions between lysosomes and mitochondria. The live-cell thermal probes provide a powerful toolbox with multimodality and multifunctional imaging capacities, including spatial, temporal, and thermal dynamics of selective organelles with high resolution and low uncertainty.

Design, Synthesis, and Characterization of Organelle-Targeted Nanothermometers

Following our previously established protocols to construct a stable and biocompatible UCNP-based nanothermometer (35, 36), $PEGMEMA_{80}$-*b*-$EGMP_3$ di-block copolymers were used to transfer hydrophobic UCNPs ($NaYF_4$: 20%Yb^{3+}, 2%Er^{3+}) into hydrophilic ones. UCNPs@copolymer showed good long-term colloidal stability in the culture medium (*SI Appendix*, Fig. S1*A*). In this design, the phosphate acid anchoring groups offer a higher affinity to lanthanide ions than oleic acid on the UCNP surface. And the carboxylic acid groups at the terminal of the $PEGMEMA_{80}$-*b*-$EGMP_3$ di-block copolymers allow further conjugation. In this work, to improve the bioconjugation efficiency of a mitochondria-targeted molecule, TPP (34), a linker molecule PLL was introduced to enrich the density of amine groups on the surface of UCNPs@copolymer through attractive electrostatic interactions. By the carbodiimide reaction, UCNPs@PLL were further cross-linked with TPP to form UCNPs@PLL@TPP that exhibited chemical stability in the culture medium (*SI Appendix*, Fig. S1*B*). The three kinds of modified nanoparticles, including UCNPs@copolymer, UCNPs@PLL, and UCNPs@PLL@TPP, showed good morphology uniformity and monodispersity (Fig. 1*A*). Measured by transmission electron microscopy (TEM), the size of nanoparticles increased from 29.97 ± 0.98 nm to 30.23 ± 1.48 nm, 30.54 ± 1.17 nm, and 31.57 ± 1.23 nm (Fig. 1*B*) after each step of surface modifications. The dynamic light scattering (DLS) results confirmed the high uniformity with the average values of hydrodynamic size increasing from 55.67 ± 0.62 nm to 59.80 ± 0.25 nm and 66.51 ± 1.49 nm (Fig. 1*C*). The zeta potential results (Fig. 1*D*) indicated the successful modifications of each step, as the surface charge turned from negative 14.28 ± 0.59 mV to positive 20.77 ± 0.30 mV with PLL and positive 12.18 ± 0.47 mV with TPP. The presence of $PEGMEMA_{80}$-*b*-$EGMP_3$ di-block copolymers, PLL, and TPP were further confirmed by Attenuated total reflectance Fourier transform infrared (ATR-FTIR) spectroscopy. As shown in *SI Appendix*, Fig. S2, after grafting the $PEGMEMA_{80}$-*b*-$EGMP_3$ di-block copolymers on the surface of the nanoparticles, the asymmetric COO− stretching at 1,547 cm^{-1} of oleic acid molecules completely disappeared, with both the characteristic ATR-FTIR spectral peak at 1,100 cm^{-1} (C−O−C stretching) and the new Ph-P band at 1,440 cm^{-1} confirming the success in $PEGMEMA_{80}$-*b*-$EGMP_3$ di-block copolymers and TPP ligand modifications.

To demonstrate the advantage of the PLL-based cascade modification strategy in this work, we compared the UCNPs@PLL with UCNPs@PEG (23). Previously, the cross-linked polymer networks are composed of $PEGMEMA_{80}$-*b*-$EGMP_3$ di-block copolymers and 4Arm-PEG-NH_2 on the surface of UCNPs (UCNPs@PEG). As shown in Fig. 1 *E* and *F* and *SI Appendix*, Fig. S3, the measurements indicated that the luminescent intensities of UCNPs@PLL are significantly higher than that of UCNPs@PEG. This may be due to the vibrational states of chemical bonds (O-H, C-H, or N-H) on the UCNPs surface that match the phonon states of the host material, resulting in nonradiative relaxation of the excited lanthanide ions (35). Moreover, compared with 4Arm-PEG-NH_2, the PLL molecules provide many more amine groups on the UCNP surface. To prove this, 10 mg of TPP and 5 mg of nanoparticles were conjugated overnight through a carbodiimide crosslinking reaction. After that, unreacted TPP was completely removed by centrifugal

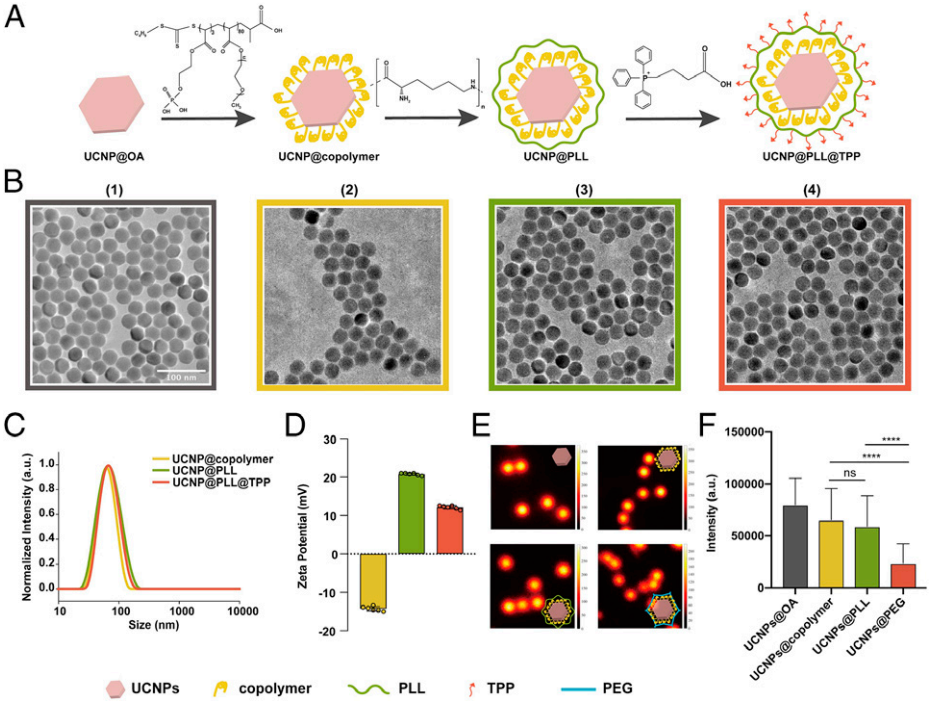

Fig. 1. Surface modification strategy and characterization of UCNPs to produce efficient organelle-targeting nanothermometers. (*A*) Schematic illustration of the cascade modification steps based on UCNPs with the surface modified from OA (pink), to $PEGMEMA_{80}$-*b*-$EGMP_3$ di-block copolymers (yellow), PLL (green), and TPP (red), respectively. (*B*) Representative TEM images of 1) UCNPs-OA (gray), 2) UCNPs@copolymer (LysoDots, yellow), 3) UCNPs@PLL (green), and 4) UCNPs@PLL@TPP (MitoDots, red), respectively. (Scale bar, 100 nm.) (*C*) DLS size analysis of UCNPs after different surface modifications (color codes same as in *B*). (*D*) ζ-Potentials of UCNPs after different surface modifications (color codes same as in B). (*E*) Luminescence emission images from individual UCNPs coated with OA, copolymer, PLL, and 4Arm-PEG-NH_2 (PEG) under 980-nm excitation, with the same experimental conditions. (*F*) Statistics of the emission intensity of single individual UCNPs in *E*. Data points represent mean ± SD. $n = 160$ single particles. Significance label, NS, no significance; ****$P < 0.0001$.

ultrafiltration and the supernatant was retained. According to the UV−visible (Vis) absorptions at 268 nm of various concentrations of TPP in the supernatant (*Materials and Methods* and *SI Appendix*, Fig. S4), the conjugation efficiency of TPP has been enhanced from 0.332 mg to 1.545 mg for 5 mg of UCNPs@PEG and UCNPs@PLL, respectively.

From here, we will refer to the UCNPs@copolymer nanoparticles as LysoDots and the UCNPs@TPP nanoparticles as MitoDots, for clearer presentation. And we will assess the thermal responsive properties, stabilities, biocompatibility, organelle-specific accumulations, and temperature monitoring capacities in the following sections.

Thermal Responsive Properties and Stabilities of LysoDots and MitoDots

The luminescence spectrum change of Yb^{3+} and Er^{3+} codoped UCNPs strongly depends on the temperature (Fig. 2*A*, section 1). Within a single nanoparticle, Yb^{3+} ions transfer the sensitized 980nm photon energy to Er^{3+} ions that upconvert the energy of multiple photons to emit two distinct temperature-responsive green emissions at 515- to 535-nm (centered at 525 nm) and 535- to 570-nm (centered at 545 nm) bands (Fig. 2*A*, section 2). The intensity ratio of 525-nm and 545-nm bands follows the Boltzmann distribution, regardless of the concentrations of nanoparticles,

$$\frac{I_{525}}{I_{545}} = Cexp\left(-\frac{\Delta E}{kT}\right), \quad [1]$$

where I_{525} and I_{545} are the integrated luminescent intensities at the 525-nm and 545-nm emission bands, respectively; C is a constant; ΔE is the $^4S_{3/2}$ to $^2H_{11/2}$ energy difference of the Er^{3+} ion; k is the Boltzmann constant; and T is the absolute temperature. The calibration curve of nanoparticles in the water was plotted showing a great linear fitting ($R^2 = 0.9757$, Fig. 2*A*, section 3).

Living cells are complex systems with the environment changing in both spatial and temporal domains. For example, the pH value is much lower in lysosomes than that in other organelles. The concentrations of Ca^{2+} in mitochondria and lysosomes also vary across the different phases of the cell cycle. To validate the temperature detection stability of LysoDots and MitoDots, we measured the temperature-dependent spectrum in different pH (4–10) and ion concentration conditions, including Ca^{2+} (0 to 2 mM), Mg^{2+} (0 to 1.2 mM), and K^+ (0 to 500 mM). Results in Fig. 2*B* and *SI Appendix*, Fig. S5 confirm that the luminescence responding to the temperature of LysoDots (Fig. 2 *B*, *Left*) and MitoDots (Fig. 2 *B*, *Right*) are independent of either ion concentration or pH conditions.

To demonstrate the advance of the cascade modification strategy in enhancing the mitochondrial targeting efficiency, both UCNPs@PLL@TPP (Fig. 2 *C*, *Top*) and UCNPs@PEG@TPP used in our previous work (23) (Fig. 2 *C*, *Bottom*) were incubated with HeLa cells for 12 h. As shown in Fig. 2*D*, the average intensity of individual foci from UCNPs@PLL@TPP (MitoDots) was almost 10 times higher than that of UCNPs@PEG@TPP. The results suggest that more TPP on the surface of UCNPs@PLL enabled the more efficient mitochondria-targeting ability of nanothermometry MitoDots.

Biocompatibility and Specificities of the Cascade Organelle-Targeting and Accumulation of LysoDots and MitoDots

We further performed biocompatibility assessment and colocalization assays in HeLa cells to evaluate the intracellular-specific localizations and organelle accumulation efficiencies of LysoDots

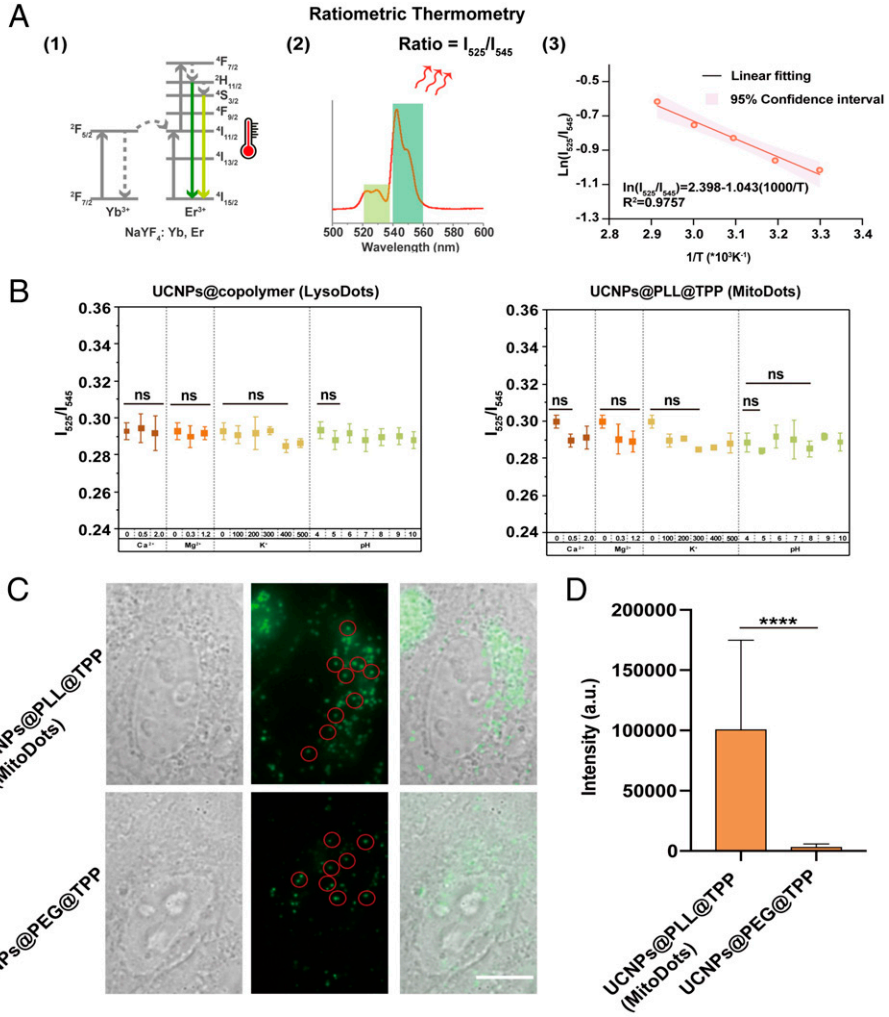

Fig. 2. Stable and efficient LysoDots and MitoDots. (*A*) Energy level (section 1) and ratiometric thermometry (section 2) of temperature-sensitive UCNPs. Standard temperature-sensing curve (section 3) by plotting $\ln(I_{525}/I_{545})$ vs. 1000/T to calibrate the thermometric scale in hydrophilic solution. The equation is $y = -1.043\times + 2.398$ ($R^2 = 0.9757$). (*B*) Stability tests of ratiometric thermometry at different Ca^{2+} ion concentrations (0 to 2 mM), Mg^{2+} ion concentrations (~0 to 1.2 mM), K^+ ion concentrations (~0 to 500 mM), and pH values (~4 to 10). $n = 3$ independent repeats. (*C*) Bright-field, luminescence, and merge images of UCNPs@PLL@TPP (MitoDots) and UCNPs@PEG@TPP in HeLa cells. (Scale bar, 10 μm.) (*D*) Quantification of enhanced emission intensities from UCNPs@PEG@TPP to UCNPs@PLL@TPP (MitoDots) used in HeLa cells. Data points represent mean ± SD. $n = 200$ regions of interest (ROIs). Significance label, NS, no significance; ****$P < 0.0001$.

and MitoDots using LysoTracker and MitoTracker as control. They were characterized on a purpose-built total internal reflected fluorescence (TIRF) microscope system with 561-nm, 647-nm, and 980-nm excitation lasers, a live cell incubator with temperature control, and an Electron Multiplying Charge-Coupled Devices (EMCCD) (see *Materials and Methods* for details).

We firstly checked the biocompatibility of LysoDots and MitoDots with the lysosomal intracellular activity assay (*SI Appendix*, Fig. S6) and the MTT (3-(4,5-dimethylthiazol-2-yl)-2,5-diphenyltetrazolium bromide, a tetrazole) assay (*SI Appendix*, Fig. S7), respectively. We demonstrate that neither LysoDots nor MitoDots affect the lysosomal, mitochondrial, and cellular functions after incubation and endocytosis in HeLa cells at 50 μg/mL. We then checked the targeting specificity of LysoDots by incubating HeLa cells with LysoDots alone for 12 h, followed by LysoTracker Red and MitoTracker DeepRed staining for 30 min before TIRF imaging. As shown in Fig. 3 *A*, *Top*, both luminescent images and line profiles demonstrate that LysoDots (cyan) colocalized cohesively with LysoTracker (magenta) and with similar dotted morphologies. The Pearson's coefficient between LysoDots and LysoTracker (Fig. 3 *B*, *Top*) was 0.95, almost twice higher than that between LysoDots and MitoTracker (0.54). Usually, we consider a Pearson's coefficient value higher than 0.6 as credible colocalizations (37).

Similarly, we then checked the specificity of MitoDots by incubating HeLa cells with MitoDots (cyan) alone for 12 h, followed by LysoTracker and MitoTracker staining. As shown in Fig. 3 *A*, *Bottom*, both luminescent images and line profiles demonstrate that MitoDots also colocalized cohesively with MitoTracker (yellow) with similar linear and network morphologies. The Pearson's coefficient values (Fig. 3 *B*, *Bottom*) between MitoDots and LysoTracker and between MitoDots and MitoTracker were 0.82 and 0.77, respectively, revealing the process of MitoDots' escape from lysosomes to mitochondria. The significantly higher Pearson's coefficient values between MitoDots and MitoTracker (0.77), compared with that between LysoDots and MitoTracker (0.54, $P < 0.001$, Fig. 3*C*), confirmed that the sufficient amount of TPP moieties on the surface of MitoDots has efficiently facilitated nanothermometers to anchor onto mitochondria.

We have also isolated lysosomes (Fig. 3*D*) and mitochondria (Fig. 3*G*) from the HeLa cells incubated with LysoDots and MitoDots, orthogonally. The accumulation of LysoDots into lysosomes and MitoDots into mitochondria were then assessed

with TIRF imaging of isolated organelles on coverglass surfaces (see *Materials and Methods* for details). As shown in Fig. 3 *E*, *F*, *H*, and *I*, the luminescent images and intensities indicate the internalization pathway of LysoDots being stuck in lysosomes and MitoDots successfully relocating from lysosomes into mitochondria. This internalization and specific accumulation process have been further revealed by time-dependent imaging and an increment in Pearson's coefficient values in *SI Appendix*, Fig. S8. As a result, in our cascade organelle-targeting strategy, after being internalized by the cells (34), UCNPs@copolymer nanoparticles (LysoDots) translocate from the early endosomes to the late endosomes that ferry the nanoparticles into lysosomes, and

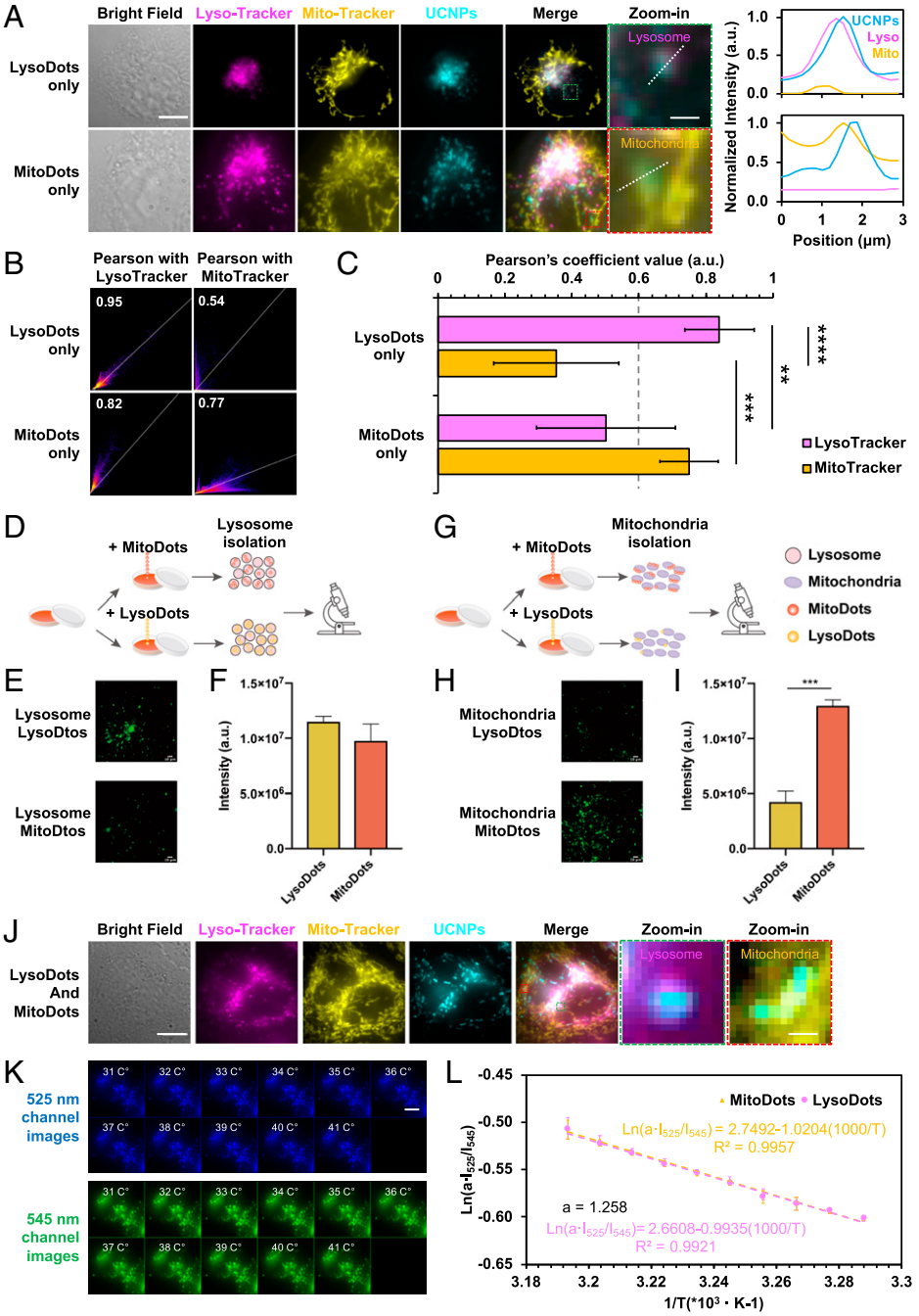

Fig. 3. Organelle-specific accumulations of LysoDots and MitoDots. (*A*) Images of representative cells were incubated with LysoDots (cyan, *Top*) or MitoDots only (cyan, *Bottom*) for 12 h followed by LysoTracker (magenta) and MitoTracker (yellow) staining for 30 min before TIRF imaging. The zoom-in areas show colocalizations and morphologies. The line profiles demonstrate colocalization across the three channels. (Scale bar, 10 μm for whole-cell images and 1 μm for the zoom-in images.) (*B*) Pearson's coefficient values of LysoDots with LysoTracker and MitoTracker (*Top*) and MitoDots with LysoTracker and MitoTracker (*Bottom*). (*C*) Statistics of Pearson's coefficient values in *B*. Data points represent mean ± SD. $n = 30$ ROIs from three independent biological experiments. Significance label $^{**}P < 0.01$; $^{***}P < 0.001$; $^{****}P < 0.0001$. (*D* and *G*) Experimental design of lysosomal isolation (*D*) and mitochondrial isolation (*G*) from HeLa cells incubated with LysoDots and MitoDots, respectively. (*E* and *H*) Luminescent images of LysoDots and MitoDots from isolated lysosomes and mitochondria on the glass surface. (*F* and *I*) Statistics of the luminescent intensity of individual LysoDots and MitoDots spots from *E* and *H*. Data points represent mean ± SD. $n = 750$ (for *F*) and 660 (for *I*) individual spots from three independent biological experiments. (*J*) Images of a representative cell incubated with both LysoDots and MitoDots (cyan) for 12 h and stained with LysoTracker (magenta) and MitoTracker (yellow) 30 min before fixation and TIRF imaging, and the zoom-in areas show the colocalization and morphology. (*K*) Snapshot images of 525-nm emission (blue, *Top*) and 545-nm emission (green, *Bottom*) from UCNPs when external temperature increased from 31 to 41 C° (1 C° as interval). (*L*) Plot of $\mathrm{Ln}(a \cdot I_{525}/I_{545})$ vs. 1,000/T to calibrate the thermometric scale of LysoDots (magenta line) and MitoDots (orange line) in HeLa cells. Data represent mean ± SD ($n = 25$ cells from three independent biological experiments). (Scale bar, 10 μm.)

therefore as a nanothermometer to naturally target lysosome; UCNPs@TPP nanoparticles (MitoDots) first being accumulated in the lysosomes, and due to the lipophilic and positive TPP moieties, can escape from endolysosomes to specifically target mitochondria.

To get an in situ calibration curve for temperature sensing, we plotted the temperature value versus the I_{525}/I_{545} ratios of LysoDots and MitoDots in paraformaldehyde (PFA)-fixed HeLa cells by changing the temperature using an external temperature-controllable incubator. As shown in Fig. 3*J*, both LysoDots and MitoDots were incubated with HeLa cells for 12 h, then cells were stained with LysoTracker and MitoTracker for 30 min and followed by PFA fixation before TIRF imaging when the temperature increased from 31 °C to 40 °C (Fig. 3*K*). Both the logarithmic values of the I_{525}/I_{545} ratio for LysoDots and MitoDots showed gradual and linear luminescence relative to the reciprocal temperature, i.e., $\mathrm{Ln}(a{\cdot}I_{525}/I_{545}) = -0.9935(1{,}000/\mathrm{T}) + 2.6608$ ($R^2 = 0.9921$) and $\mathrm{Ln}(a{\cdot}I_{525}/I_{545}) = -1.0204(1{,}000/\mathrm{T}) + 2.7492$ ($R^2 = 0.9957$), respectively. Here, $a = 1.258$ is a constant to indicate the effects from in vitro to in situ conditions, such as intracellular refractive index difference, etc. As shown in Fig. 3*L*, the rmsd of these two linear fittings was measured as 0.0070, indicating no difference between LysoDots and MitoDots. The relative sensing sensitivity at 32 °C is 2.7% K^{-1} and the temperature resolution (uncertainty) is ∼0.8 K.

Spatiotemporally Mapping the Temperature Dynamics of Lysosomes and Mitochondria under Chemical Stimulations

By incubating HeLa cells with both LysoDots and MitoDots for 12 h and with LysoTracker and MitoTracker for 30 min, we simultaneously mapped the temperature dynamics of both lysosomes and mitochondria under external chemical stimulations, including organelle-nonspecific and organelle-specific treatments, which do not affect the nanothermometer performance (*SI Appendix*, Fig. S9).

We first treated HeLa cells with Ca^{2+} ion shock, which is an organelle-nonspecific treatment. The Ca^{2+} ion shock can promote the pumping of ions and accelerate respiration reactions (38). Ionomycin calcium salt is an ionophore that makes the cell membrane highly permeable for Ca^{2+} ions (21), which induces intracellular stress, possibly causing damage to both lysosomes and mitochondria in HeLa cells (38). As shown in Fig. 4 *A*–*C*, upon a 1-μM ionomycin calcium salt treatment, the lysosomal and mitochondrial temperatures first sharply increased by ∼2 to 3 °C within 6 min before dropping back together in the next 20 min (Fig. 4*B*). As a solvent control, the temperature remained at a relatively stable level regardless of the addition of 1:1,000 dimethyl sulfoxide (DMSO) into the culture media (Fig. 4*C*).

Next, we treated live cells with a lysosome-specific CQ stimulation (Fig. 4*D*). CQ has originally been used to treat malaria and is now a sensitizing agent to treat certain cancers (39). CQ is a lysosomotropic weak base, which increases the pH of lysosomes and therefore inhibits autophagic degradation in the lysosomes (40). Intriguingly, the nanothermometry measurements by LysoDots and MitoDots revealed a significant decrease in lysosomal temperature by ∼3 °C after a 10-min treatment of 200 nM CQ, while the mitochondrial temperature remained relatively stable as the basal level in HeLa cells (Fig. 4*E*). In comparison, the temperature in the solvent treatment groups remained at a relatively stable level after adding phosphate-buffered saline (PBS) to the culture media (Fig. 4*E*).

We then treated HeLa cells with a mitochondria-specific drug, carbonyl cyanide-4-(trifluoromethoxy)phenylhydrazone (FCCP) (Fig. 4*F*). FCCP is an inhibitor of mitochondrial oxidative phosphorylation, as it disrupts ATP synthesis by transporting protons across the mitochondrial inner membrane (41). LysoDots and MitoDots not only revealed a significant increase of both the lysosomal and mitochondrial temperature by almost ∼3 to 7 °C in the first 10 min after adding 10 μM FCCP ($P < 0.0001$ by Student's t test, Fig. 4*G*), but also mitochondria release a large amount of heat, which is consistent with the previous observation (23), but with better uncertainty using MitoDots. Here, a clear delay by ∼1 to 2 min in the time domain during the process of both temperature increase (0 to 6 min) and decrease (10 to 14 min) between lysosomes and mitochondria has been demonstrated (Fig. 4*G*). The significant temperature increase reflects a large amount of heat released by mitochondria, with the trend being consistent with the previous observation (23). The ability of MitoDots suggests better temperature-sensing uncertainty, and the observation of time delays further indicates a thermal transition from mitochondria to the lysosomes. In the following 20 min, the lysosomal and mitochondrial temperature eventually recovered to the original temperature, but the cellular morphology significantly changed, indicating cell death after mitochondrial dysfunction. In addition, the heterogeneous thermogenesis of lysosomes and mitochondria has been demonstrated in *SI Appendix*, Fig. S10 at different time points.

Conclusion and Discussion

The intracellular thermal dynamics, as one of the most pivotal biophysical parameters, plays a critical role in maintaining the cells' homeostasis or driving the cells into dysfunction status. With the advances made in noncontact luminescent nanothermometers, a wide variety of intracellular nanothermometers has been developed and applied to monitor organelle temperature variations (25). Previous literature reports have been briefly summarized in Table 1, indicating that the mitochondrial temperature increases in the range from 2 to 10 °C under biochemical stimulations. The advantages of LysoDots and MitoDots are their simultaneous nonphotobleaching property, better uncertainty, and multiple organelle-targeting strategy. In our work, the temperature of mitochondria increases 3 to 7 °C after adding FCCP, which agrees with previous observations but disagrees with the physical model of heat transfer. The theory calculations suggest that heat gradients across cells could not be greater than 10^{-5} K (49, 50). The physical models also assume that mitochondria are membrane-bound spheres and heat is produced across the surface of the spheres (49, 51). However, mitochondria are tubular and networking morphologies with double bilayered membranes (52). The heat production occurs across the cristae membranes, which typically lie in parallel, potentially retaining heat within the matrix (53). Moreover, mitochondria are highly dynamic with fission and fusion. The components of the mitochondrial inner membrane are full of cardiolipin, which is different from the cell membrane (52). This is probably another reason that mitochondria can retain heat better than smaller individual compartments (53). Additionally, the exact locations of thermal probes in living cells also affect the validity of temperature measurements. Following the typical endocytosis internalizations of nanoparticles (34), both types of nanothermometers are first accumulated into endosomes and translocated to lysosomes (Fig. 3 and *SI Appendix*, Fig. S8). The large amount of TPP on the surface of MitoDots would facilitate themselves to escape from lysosomes and attach to mitochondrial

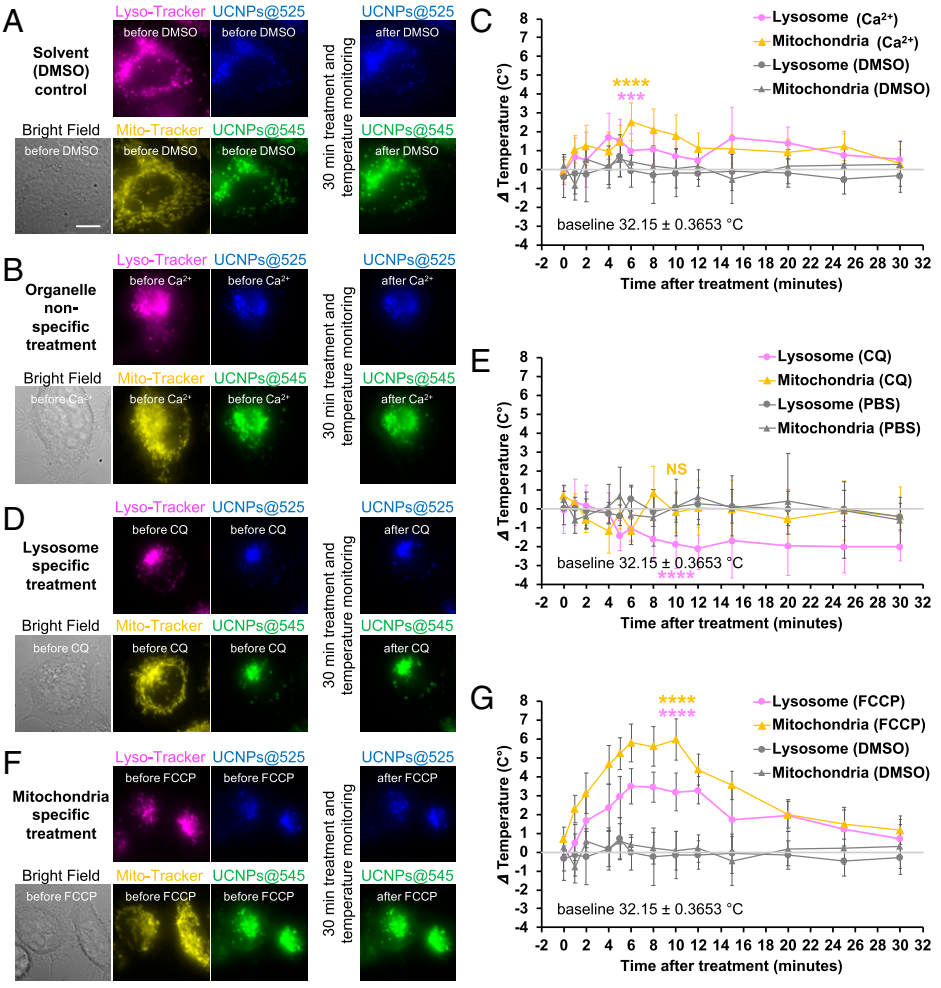

Fig. 4. Distinct lysosomal and mitochondrial temperature dynamics in response to chemical stimulations in living HeLa cells. (*A* and *B*) Bright-field (gray), LysoTracker (magenta), MitoTracker (yellow), 525-nm (blue), and 545-nm (green) emission of UCNPs images of a representative live HeLa cell before and after the treatment with 1:1,000 DMSO as the solvent control (*A*) and Ca^{2+} ion shock (*B*). (Scale bar, 10 μm.) (*C*) The temperature dynamic curves of lysosomes with Ca^{2+} ion shock (magenta circles), mitochondria with Ca^{2+} ion shock (orange triangles), lysosomes with DMSO (control, gray circles), and mitochondria with DMSO (control, gray triangles) within 30 min after treatment. Data represent mean ± SD (n = 15 ROIs from five cells) and Student's t test at 6 min (***$P < 0.001$; ****$P < 0.0001$). (*D*) Bright-field (gray), LysoTracker (magenta), MitoTracker (yellow), 525-nm (blue), and 545-nm (green) emission of UCNPs images of a representative live HeLa cell before and after the treatment with 200 nM CQ. (*E*) The temperature dynamic curves of lysosomes with CQ (magenta circles), mitochondria with CQ (orange triangles), lysosomes with PBS (control, gray circles), and mitochondria with PBS (control, gray triangles) within 30 min after treatment. Data represent mean ± SD (n = 15 ROIs from five cells) and Student's t test at 10 min (NS, no significance; ****$P < 0.0001$). (*F*) Bright-field (gray), LysoTracker (magenta), MitoTracker (yellow), 525-nm (blue), and 545-nm (green) emission of UCNPs images of a representative live HeLa cell before and after the treatment with 10 μM FCCP. (*E*) The temperature dynamic curves of lysosomes with FCCP (magenta circles), mitochondria with FCCP (orange triangles), lysosomes with DMSO (control, gray circles), and mitochondria with DMSO (control, gray triangles) within 30 min after treatment. Data represent mean ± SD (n = 15 ROIs from five cells) and Student's t test at 10 min (****$P < 0.0001$).

outer membrane surfaces or penetrate the potential barrier of the mitochondrial intermembrane (54). Thus, the generated heat from the lysosomes or mitochondria is transferred from the organelles' membrane to the temperature probes directly, which bypasses the cytosol. It can also be speculated that the temperature of the mitochondrial membrane is higher than that of cytosol and changes discontinuously at the interface. Such a discontinuity may explain the controversy between experimental results and physical calculations.

In living cells, the energy is utilized to maintain the high-dimensional structures, such as membranes, proteins, and nucleic acids, and also to control chemical reactions (55). For example, the heat generated by enzymatic reactions is commonly used for the diffusion of the enzymes themselves (56). Besides, the temperature-sensitive heat shock proteins within a living cell will initially respond to the environmental temperature changes. With a 5 to 20 °C increase in temperature, Richter et al. observed the overexpression of heat shock proteins (57). At present, researchers have started to identify the molecular mechanism in intracellular temperature regulation, but it is still unknown how the generated heat is dissipated as other types of energy or through heat conduction. Therefore, more efforts have to be put into studying the dissipation of energy converted from heat as well as the heat conduction in living cells.

The ability in mapping the distinct temperature dynamics highlights the extensive range of applications using the organelle-targeting strategy to study the vital biological processes, among lysosome (4), mitochondria (23), endoplasmic reticulum (58), Golgi apparatus (59), lipid droplet, peroxisome (13), etc. The unique properties of UCNPs, which have also been used to sense the in situ pH values (60), make it feasible to develop "all-in-one" nanoscale sensors to simultaneously monitor the pH dynamics. The time-dependent colocalization analysis in Fig. 3 and *SI Appendix*, Fig. S8 suggests the amount of MitoDots being stuck in the lysosome after an 8-h incubation was not negligible; additional rational design strategies,

Table 1. Mitochondrial temperature variation summary by intracellular thermometer

	Thermometers	Specificity	Relative sensitivity (%/°C)	Uncertainty (°C)	Photo-bleaching	Stimulations	ΔT	Ref.
Fluorescent proteins	tsGFP1-mito	Yes	N/A	N/A	Yes	FCCP Rotenone	~6 °C Decrease	(42)
	gTEMP	Yes	2.6	0.4	Yes	FCCP	~6–9 °C	(17)
	emGFP-mito	Yes	2.5	0.26	Yes	FCCP	~3–5 °C	(16)
Organic dyes	Mito-RTP	Yes	2.72	0.6	Yes	FCCP	~3 °C	(43)
	MTY	Yes	N/A	N/A	Yes	Respiration activation	~10 °C	(44)
	Mito-TEM	Yes	6.65	N/A	Yes	PMA	~3 °C	(14)
Polymeric nanoparticle		Yes	N/A	<0.98 ± 0.08	Yes	FCCP Ca^{2+}	~2.4 °C ~2 °C	(45)
		No	N/A	~0.18–0.58	Yes	FCCP	1.02 ± 0.17	(46)
		No	N/A	~0.05–0.54	Yes	CCCP	1.57 ± 1.41	(47)
Inorganic nanoparticles	Quantum dots	No	6.2	0.098	Blinking	CCCP	0.94	(48)
	UCNPs	Yes	3.2	2.3	No	FCCP Ca^{2+}	~2 °C ~3.3 °C	(23)
	LysoDots MitoDots	Yes (multiple)	2.7	0.8	No	FCCP CQ Ca^{2+}	~3–7 °C ~0 °C ~2–4 °C	This study

MTY, Mito Thermo Yellow; Ca^{2+}, ionomycin calcium; CCCP, carbonyl cyanide 3-chlorophenylhydrazone; PMA, phorbol 12-myristate-13-acetate; FCCP, carbonyl cyanide-4-(trifluoromethoxy)phenylhydrazone; CQ, chloroquine; UCNPs, upconversion nanoparticles: $NaYF_4$: Yb^{3+}, Er^{3+}.

e.g., introducing alternative small molecules, are needed to further improve the escape efficiency of MitoDots, besides enriching the density of TPP demonstrated in this work. At least, this work suggests the cascade modification and bioconjugation strategy can target other organelles and establish a library of organelle-targeted nanothermometers.

In summary, we observed the temperature decrease in lysosomes under CQ treatment and the thermal transition from mitochondria to lysosomes under FCCP stimulation. To better reveal the thermal transmission across multiple organelles, it becomes critical to further increase the spatial and temporal resolutions of our imaging system (61), so that the new series of nanothermometers can be used to map the long-term thermal dynamics of individual organelles across cell cycles or even in deep tissues (62) with single-particle sensitivity and resolution. Introducing the state-of-the-art in situ organelle imaging and assay approaches, including live-cell superresolution imaging (63, 64), in vitro reconstitution assay (52, 65), and near-infrared deep tissue imaging (66, 67), and adoptions of the new developments of live-cell nanothermometry, membrane potential sensors and pH probes will together form a powerful platform for multifunctional imaging, sensing (68), therapy (66), and even tracking the pace of life (69) in living cells and organisms.

Materials and Methods

Reagents and Materials. Yttrium(III) chloride hexahydrate ($YCl_3 \bullet 6H_2O$, 99.99%), ytterbium chloride hexahydrate ($YbCl_3 \bullet 6H_2O$, 99.99%), erbium chloride hexahydrate ($ErCl_3 \bullet 6H_2O$, 99.9%), ethanol, cyclohexane, 1-octadecane (ODE), and oleic acid (OA) were purchased from Sigma-Aldrich. $PEGMEMA_{80}$-*b*-$EGMP_3$ di-block copolymer (polymer) was synthesized as previously described (36). Poly-l-lysine (PLL), (3-carboxypropyl)triphenylphosphonium bromide (TPP), 1-Ethyl-3-(3-dimethylamino-propyl)-carbodiimide (EDC), N-hydroxysuccinimide (NHS), MES buffer, Hepes buffer, tetrahydrofuran (THF), N, N-dimethylformamide (DMF), bovine serum albumin (BSA), dimethyl sulfoxide (DMSO), carbonyl cyanide-4-(trifluoromethoxy)phenylhydrazone (FCCP), and ionomycin calcium salt were purchased from Sigma-Aldrich with reagent grade or higher. Dulbecco's modified Eagle medium (DMEM), fetal bovine serum (FBS), phosphate-buffered saline (PBS), penicillin-streptomycin (PS), LysoTracker (LysoTracker Deep Red FM, Invitrogen L12492), MitoTracker (MitoTracker Deep Red FM, Invitrogen M22426), and mitochondria isolation kit for cultured cells (89874) were purchased from Life Technologies (Thermo Fisher). Chloroquine (CQ, 14774S) was purchased from Cell Signaling Technology. Deionized (DI) water was generated by Milli-Q IQ Water Purification System (Millipore). The Lysosome Isolation Kit (ab234047) and the Lysosomal Intracellular Activity Assay Kit (ab234622) were purchased from Abcam.

Synthesis of Hydrophilic UCNPs. $NaYF_4$: 20%Yb^{3+}, 2%Er^{3+} nanoparticles were synthesized following the previously reported protocols with some modification (23, 70). As in a typical process, stock solutions of YCl_3 (0.4 M), $YbCl_3$ (0.2 M), and $ErCl_3$ (0.1 M) were prepared freshly. Then, 6 mL of OA and 15 mL of ODE were added into a 50-mL round bottom flask with three necks, and then 1.95 mL of YCl_3 stock solution was added, along with 1.0 mL of $YbCl_3$ stock solution and 0.2 mL of $ErCl_3$ stock solution. The mixture was stirred under argon protection and then heated to 100 °C for 10 min and 160 °C for 30 min to get rid of the methanol and H_2O. Then, 5 mL of NaOH (0.1 g)–NH_4F (0.14815 g) methanol solution was added to the mixture until it cooled down to 30 °C and stirred for 30 min. Subsequently, the mixture was heated to 100 °C for 30 min and then heated to 300 °C for 1 h. Finally, 5 mL of ethanol was added to the mixture to precipitate UCNPs. UCNPs were washed three times with ethanol and cyclohexane before use. Finally, the UCNPs were dissolved in 10 mL of cyclohexane and stored in the fridge.

To obtain hydrophilic UCNPs, the nanoparticles were first modified with $PEGMEMA_{80}$-*b*-$EGMP_3$ di-block copolymer (polymer) (71). A total of 5 mg of UCNPs and 5 mg of polymer were dissolved in 1 mL of THF and then shaken at room temperature for 12 h. Next, the UCNPs coated with polymers (UCNPs@polymer) were washed with THF three times and DI water three times. Finally, the UCNPs@polymer was dissolved in 0.5 mL of DI water and stored at 4 °C for further use.

Bioconjugation of UCNPs with TPP. To functionalize hydrophilic nanoparticles with amine groups, 0.5 mL of UCNPs@polymer was dissolved in the 0.5 mL of PLL solution and stirred at room temperature for 40 min. The reaction was stopped by centrifugation and washed three times with DI water. Finally, the UCNPs functionalized with amine groups (UCNPs@PLL) were stored at 4 °C for further use.

For the bioconjugation of UCNPs@PLL with TPP, 30 mg of TPP, 10 mg of EDC, and 10 mg of NHS were first dissolved into 1 mL of DMF by ultrasound. After 1 h, 10 mg of UCNPs@PLL was added to the mixture. The reaction was stirred at room temperature for 12 h and then washed with DMF and DI water. Finally, the product UCNPs@PLL conjugated with TPP (UCNPs@TPP) was stored in 0.5 mL of DI water at 4 °C for further use.

UCNP Morphology Characterization. The morphology of UCNPs was characterized using the FEI Tecnai TEM. The hydrodynamic size and zeta potential of UCNPs were determined by a zeta sizer nano (Malvern). The spectra were measured by a custom-built spectrometer.

The Luminescent Intensity Measurement of Individual UCNPs. The luminescent intensity of individual UCNPs was measured by a purpose-built scanning confocal system, with an excitation laser at 980 nm, which is focused onto the sample through a 100× objective lens (numerical aperture [NA] 1.4). The emission of UCNPs ($NaYF_4$: 20%Yb^{3+}, 2%Er^{3+}) was collected by the same objective lens, then focused by a tube lens to an optical fiber. A single-photon counting avalanche diode (SPAD) detector was connected to the optical fiber to detect the emission intensity. The scanning is achieved by the *x-y* movement of the three-dimensional piezo stage. After the point-by-point scanning process, each single UCNP ($NaYF_4$: 20%Yb^{3+}, 2%Er^{3+}) presented a Gaussian spot in the confocal scanning microscope image. The maximum brightness value (photon count) of each Gaussian spot can be used to represent the intensity of a single particle.

Luminescent Stability of UCNPs@TPP Against Environmental Parameters. The spectrometer was used to measure the emission spectrum of LysoDots or MitoDots under different pH, ionic strength (Mg^{2+}, Ca^{2+}, and K^{+}) and drugs (CQ and FCCP). The PBS with gradient pH values (4–10) was tuned by adding different amounts of HCl or KOH. Ionic strength (0 to 500 mM KCl) was controlled by adding different amounts of KOH. The 0 to 2.0 mM $CaCl_2$, and 0 to 1.2 mM $MgCl_2$ were obtained by adding different amounts of $CaCl_2$ and $MgCl_2$. A total of 1 mg of LysoDots or MitoDots was dissolved in the PBS with different pH, different concentrations of ionic strength, or drugs, and transferred to the cuvette. The samples were excited at 980 nm and the spectrum was captured from 480 nm to 600 nm.

Cell Culture, Labeling, and Colocalization of UCNPs with MitoTracker and LysoTracker. HeLa cells were purchased from ATCC. The HeLa cells were seeded on the fluoro-dish (35 mm) at 10^5 cell counting/density and incubated in the DMEM containing 10% vol/vol FBS for 12 h. Then the cells were washed three times with PBS and incubated with UCNPs (50 μg/mL, 1 mL) for 12 h at 37 °C with 5% CO_2. Next, the cells were washed with PBS and incubated with 200 nM MitoTracker and/or 200 nM LysoTracker for 0.5 h in DMEM. Finally, the cells were washed with PBS and incubated in DMEM for TIRF imaging.

Cytotoxicity Assay (MTT Assay). HeLa cells were purchased from ATCC. First of all, 5 mg of MTT was dissolved into 1 mL of sterile PBS buffer. Then 10,000 cells were seeded in the 96-well plate. UCNPs with different modifications (50 μg/mL) were added to each well. Then fresh culture medium was added to the plate after 24 h. A total of 10 μL of MTT stock solution was added to each well. This 96-well plate was kept in a 37 °C incubator for another 4 h. Finally, 50 μL of DMSO was added to each well. The microplate reader (Infinite M200 PRO, Tecan) was applied to read the absorbance at 540 nm.

Mitochondria Isolation and Fluorescence Intensity Analysis. Mitochondria from HeLa cells were isolated by a kit purchased from Thermo Fisher by following the manufacturer's manual. The protease inhibitors were added to Reagent A and Reagent C before starting the experiment. The 2×10^7 cells were cultured in two T175 flasks and treated with 50 μg/mL UCNPs@copolymer, UCNPs@PEG, and UCNPs@TPP for 12 h, respectively. Then 2×10^7 cells were collected by centrifugation. A total of 800 μL of Reagent A was added to the cell pellet and vortexed at medium speed for 5 s. The cell suspension was put on ice for exactly 2 min. Next, 10 μL of Reagent B was added to the cell suspension and vortexed at maximum speed for 5 s. The mixture was incubated on ice for another 5 min. After 800 μL of Reagent C was added to the cell suspension, the mixture was centrifuged at 700 × *g* for 10 min at 4 °C. Then the supernatant was transferred to a new tube and centrifuged at 12,000 × *g* for 15 min at 4 °C. The cell pellet was dissolved in 500 μL of Reagent C and centrifuged at 12,000 × *g* for 5 min. Finally, the pellet was resuspended in 50 μL PBS buffer and transferred to a 96-well plate. The fluorescence intensity was recorded by a homemade TIRF microscope with an excitation wavelength of 980 nm.

Lysosome Isolation and Fluorescence Intensity Analysis. Lysosomes from HeLa cells were isolated by a kit bought from Abcam. Briefly, following the manufacturer's manual, 2×10^7 cells were collected by centrifugation at 600 × *g* for 10 min. A total of 500 μL of lysosome isolation buffer was added to the pellet and vortex for 5 s, followed by incubation on ice for 2 min. Then the cells were homogenized using a precooled glass Dounce homogenizer. The sample was stroked 20 to 30 times on ice and transferred to a fresh tube. A total of 500 μL of lysosome enrichment buffer was added to the sample. The tube was inverted several times to mix. Next, the sample was centrifuged at 500 × *g* for 10 min at 4 °C and the supernatant was collected in a separate tube and kept on ice. The lysosome gradient/lysosome enrichment gradient solutions were prepared in an ultracentrifuge tube according to the manufacturer's manual. The cell lysate was added to the top of the prepared density gradient carefully. Then the sample was centrifuged using an ultracentrifuge for 2 h at 145,000 × *g* at 4 °C. The lysosome band was visible in the top 1/10th of the gradient volume. The lysosome fraction band was withdrawn carefully by using an extralong pipette tip (~0.2 mL) starting from the top of the gradient. This fraction contains enriched lysosomes. To further purify, this fraction was mixed with two volumes of PBS and vortexed gently. Finally, the sample was centrifuged for 30 min at 18,000 × *g* at 4 °C. The pellet containing the purified lysosomes was resuspended in the 50 μL of PBS buffer and transferred to a 96-well plate. The luminescence intensity was recorded by a homemade TIRF microscope with an excitation wavelength of 980 nm.

Lysosomal Intracellular Activity Assay. HeLa cells were purchased from ATCC. The lysosomal activity was tested by a kit bought from Abcam. Briefly, the HeLa cells were seeded on the fluoro-dish (35 mm) at the cell density of 10^5 cells/mL and incubated in the DMEM containing 10% vol/vol FBS for 12 h. The next day, the culture medium was removed and replaced with a fresh complete medium containing UCNPs with different modifications (50 μg/mL). For experimental control, 1,000× Bafilomycin A1 stock was directly diluted into the media to obtain the 1× final concentration. The cells were incubated for 12 h, at 37 °C with 5% CO_2. Upon completion, the medium was replaced with fresh aliquots supplemented with 0.5% FBS containing UCNPs with different modifications (50 μg/mL). For experimental control, Bafilomycin A1 was diluted to 1× final concentration. In 1 mL culture media, 15 μL of self-quenched substrate was added into the positive control, experimental control and cells treated with UCNPs nanoparticles. The cells were incubated at 37 °C with 5% CO_2 for 1 h. Next, the cells were washed with 1 mL ice-cold 1× assay buffer containing nanoparticles or Bafilomycin A1 at the same concentration. For flow cytometer analysis, the cells were collected at 300 × *g* for 5 min at room temperature and resuspended in 1 mL of 1× PBS containing the nanoparticles or Bafilomycin A1. Cells were ready to be analyzed on a flow cytometer (488-nm excitation laser). For fluorescence microscope analysis, the cells were imaged under a fluorescence microscope with a 488-nm excitation filter.

Time-Dependent Localization/Accumulation of LysoDots and MitoDots. To track the intracellular fate of the LysoDots and MitoDots after being internalized by the cells, the time-dependent location/accumulation of LysoDots and MitoDots were characterized, respectively. HeLa cells were cultured in the glass-bottomed dish and incubated with LysoDots or MitoDots for 2, 4, 6, and 8 h. Then the cells were stained with LysoTracker DeepRed or MitoTracker DeepRed for 30 min right before the TIRF imaging. The cell samples were imaged with dual-color TIRF microscopy at the wavelengths of 980 nm and 647 nm.

Relative Temperature-Sensing Sensitivity and Uncertainty. The relative temperature-sensing sensitivity (S_r) indicates the relative change of Δ per degree of temperature change and was calculated using ref. 72:

$$S_r = \frac{1}{\Delta}\left|\frac{\partial \Delta}{\partial T}\right|. \quad [2]$$

The temperature uncertainty δT is the smallest temperature change that can be detected in a given measurement and was defined by ref. 72:

$$\delta T = \frac{\delta \Delta}{S_r \cdot \Delta}. \quad [3]$$

In Situ Calibration Curves and Temperature Sensing of Lysosomes and Mitochondria. The HeLa cells were cultured in DMEM containing 10% vol/vol FBS and 1% vol/vol penicillin-streptomycin at 37 °C with 5% CO_2. Cells were transferred into the fluoro-dish (35 mm in diameter with No. 1 coverglass bottom). Then the cells were incubated in the dish with 1 mL culture medium

containing 50 μg/mL UCNPs@PLL (LysoDots) and/or UCNPs@TPP (MitoDots) at 37 °C for 12 h.

To obtain the in situ calibration curves for temperature sensing inside HeLa cells, the LysoDots- and MitoDots-labeled cells were fixed by 4% PFA and imaged immediately afterward on a custom-built TIRF microscope with an external temperature controller. The calibration curves for LysoDots (magenta dots and linear fit, Fig. 3*L*) and MitoDots (orange dots and linear fit, Fig. 3*L*) were separately obtained by a 980-nm laser excitation and 525/545-nm emission under different temperatures (from 31 °C to 40 °C with 1 °C as the interval). The calibration curves were plotted as $y = Ax + B$, where y is $\mathrm{Ln}(a \cdot I_{525}/I_{545})$, x is 1,000/T, and a is the constant to indicate the cellular and system effects, compared with in vitro conditions in Fig. 2*A*, section 3, such as the refractive index changes in cytoplasm, the band-pass filter sets we used to measure I_{525} and I_{545}, etc. And this constant "*a*" should be different with different cell types and microscopy setups. Here in this study, $a = 1.258$.

For the CQ-, FCCP-, and Ca^{2+}-induced lysosomal and mitochondrial temperature changes in Fig. 4, firstly, the LysoDots and MitoDots were incubated with HeLa cells for 12 h (overnight). Then, the HeLa cells were stained with LysoTracker Red and MitoTracker Deep Red following the manufacturer's instructions. Next, PBS (as solvent control), DMSO (1:1,000 as solvent control), CQ (200 nM), FCCP (10 μM), or ionomycin calcium salt (1 μM) was incubated with HeLa cells before and during the TIRF imaging. The fluorescence intensities of LysoTracker Red and MitoTracker Deep Red were excited with 561-nm and 647-nm lasers (MPB Communication) and the emissions were detected with 593/40 and 680/42 emission filters (Semrock), respectively. The luminescent intensities and ratio (I_{525}/I_{545}) of LysoDots and MitoDots were excited with a 980-nm laser (Thorlabs) and detected by 525/15 and 545/30 emission filters (Semrock), respectively. All the fluorescent and luminescent signals were detected by an EMCCD (DU897, Andor).

For data analysis, the raw images were input into ImageJ (Fiji) and luminescent intensities of single particles were analyzed with measurement tools. For lysosomal and mitochondrial temperature monitoring, $\mathrm{ln}(I_{525}/I_{545})$ values of LysoDots and MitoDots were calculated for those UCNPs only colocalized with LysoTracker and MitoTracker, respectively. Then the in situ temperature dynamics of lysosomes and mitochondria were determined according to the calibration curves of LysoDots and MitoDots in Fig. 3*L*, respectively, and then plotted in Fig. 4 *C*, *E*, and *G*.

Statistical Analysis. The Student's *t* test was applied to examine the differences among variables. Data are shown as mean ± SD. **P* values ≤0.05 are considered to be statistically significant.

Data, Materials, and Software Availability. Materials and methods details, synthesis of UCNPs, the data analysis process, biostability of nanoparticles, ATR-FTIR spectra, luminescence emission images of UCNPs, UV–Vis standard curve of TPP, lysosomal intracellular activity assay, MTT assay, and heterogeneous thermogenesis can be found in the supporting information. All other study data are included in the article.

ACKNOWLEDGMENTS. We acknowledge the financial support from the Australia National Health and Medical Council (APP1177374 to Q.P.S.), the Australia National Heart Foundation (102592 to Q.P.S.), the National Natural Science Foundation of China (NSFC, 61729501), the Major International (Regional) Joint Research Project of NSFC (51720105015), the Science and Technology Innovation Commission of Shenzhen (KQTD20170810110913065), the Australia–China Science and Research Fund Joint Research Centre for Point-of-Care Testing (ACSRF658277 and SQ2017YFGH001190), the Australian Research Council Laureate Fellowship Program (D.J., FL210100180), and the China Scholarship Council (201706170028 to X.D. and 201706170027 to D.W.).

Author affiliations: [a]Institute for Biomedical Materials and Devices, Faculty of Science, University of Technology Sydney, Sydney, NSW 2007, Australia; [b]School of Biomedical Engineering, Faculty of Engineering and Information Technology, University of Technology Sydney, Sydney, NSW 2007, Australia; and [c]UTS-SUStech Joint Research Centre for Biomedical Materials and Devices, Department of Biomedical Engineering, Southern University of Science and Technology, Shenzhen, Guangdong 518055, China

1. Z. Huang, N. Li, X. Zhang, Y. Xiao, Mitochondria-anchored molecular thermometer quantitatively monitoring cellular inflammations. *Anal. Chem.* **93**, 5081–5088 (2021).
2. J. Zhou, B. Del Rosal, D. Jaque, S. Uchiyama, D. Jin, Advances and challenges for fluorescence nanothermometry. *Nat. Methods* **17**, 967–980 (2020).
3. C. M. Deus, K. F. Yambire, P. J. Oliveira, N. Raimundo, Mitochondria-lysosome crosstalk: From physiology to neurodegeneration. *Trends Mol. Med.* **26**, 71–88 (2020).
4. W. Du *et al.*, Kinesin 1 drives autolysosome tubulation. *Dev. Cell* **37**, 326–336 (2016).
5. M. Audano, A. Schneider, N. Mitro, Mitochondria, lysosomes, and dysfunction: Their meaning in neurodegeneration. *J. Neurochem.* **147**, 291–309 (2018).
6. L. F. Burbulla *et al.*, Dopamine oxidation mediates mitochondrial and lysosomal dysfunction in Parkinson's disease. *Science* **357**, 1255–1261 (2017).
7. J. M. Mc Donald, D. Krainc, Lysosomal proteins as a therapeutic target in neurodegeneration. *Annu. Rev. Med.* **68**, 445–458 (2017).
8. Q. P. Su *et al.*, Vesicle size regulates nanotube formation in the cell. *Sci. Rep.* **6**, 24002 (2016).
9. Q. Wan, S. Chen, W. Shi, L. Li, H. Ma, Lysosomal pH rise during heat shock monitored by a lysosome-targeting near-infrared ratiometric fluorescent probe. *Angew. Chem. Int. Ed. Engl.* **53**, 10916–10920 (2014).
10. J. R. Friedman, J. Nunnari, Mitochondrial form and function. *Nature* **505**, 335–343 (2014).
11. F. Baixauli *et al.*, Mitochondrial respiration controls lysosomal function during inflammatory T cell responses. *Cell Metab.* **22**, 485–498 (2015).
12. N. Plotegher, M. R. Duchen, Mitochondrial dysfunction and neurodegeneration in lysosomal storage disorders. *Trends Mol. Med.* **23**, 116–134 (2017).
13. A. M. Valm *et al.*, Applying systems-level spectral imaging and analysis to reveal the organelle interactome. *Nature* **546**, 162–167 (2017).
14. Z. Huang, N. Li, X. Zhang, C. Wang, Y. Xiao, Fixable molecular thermometer for real-time visualization and quantification of mitochondrial temperature. *Anal. Chem.* **90**, 13953–13959 (2018).
15. R. Kriszt *et al.*, Optical visualisation of thermogenesis in stimulated single-cell brown adipocytes. *Sci. Rep.* **7**, 1383 (2017).
16. O. A. Savchuk, O. F. Silvestre, R. M. R. Adão, J. B. Nieder, GFP fluorescence peak fraction analysis based nanothermometer for the assessment of exothermal mitochondria activity in live cells. *Sci. Rep.* **9**, 7535 (2019).
17. M. Nakano *et al.*, Genetically encoded ratiometric fluorescent thermometer with wide range and rapid response. *PLoS One* **12**, e0172344 (2017).
18. S. Uchiyama, C. Gota, T. Tsuji, N. Inada, Intracellular temperature measurements with fluorescent polymeric thermometers. *Chem. Commun. (Camb.)* **53**, 10976–10992 (2017).
19. Y. Wu *et al.*, Nanodiamond theranostic for light-controlled intracellular heating and nanoscale temperature sensing. *Nano Lett.* **21**, 3780–3788 (2021).
20. F. Pedroza-Montero *et al.*, Thermometric characterization of fluorescent nanodiamonds suitable for biomedical applications. *Appl. Sci. (Basel)* **11**, 4065 (2021).
21. J.-M. Yang, H. Yang, L. Lin, Quantum dot nano thermometers reveal heterogeneous local thermogenesis in living cells. *ACS Nano* **5**, 5067–5071 (2011).
22. C. A.-O. Brites *et al.*, Instantaneous ballistic velocity of suspended Brownian nanocrystals measured by upconversion nanothermometry. *Nat. Nanotechnol.* **11**, 851–856 (2016).
23. X. Di *et al.*, Quantitatively monitoring *in situ* mitochondrial thermal dynamics by upconversion nanoparticles. *Nano Lett.* **21**, 1651–1658 (2021).
24. K. Okabe, S. Uchiyama, Intracellular thermometry uncovers spontaneous thermogenesis and associated thermal signaling. *Commun. Biol.* **4**, 1377 (2021).
25. T. Bai, N. Gu, Micro/nanoscale thermometry for cellular thermal sensing. *Small* **12**, 4590–4610 (2016).
26. M. Suzuki, T. Plakhotnik, The challenge of intracellular temperature. *Biophys. Rev.* **12**, 593–600 (2020).
27. R. Piñol *et al.*, Real-time intracellular temperature imaging using lanthanide-bearing polymeric micelles. *Nano Lett.* **20**, 6466–6472 (2020).
28. D. B. Ambiliraj, B. Francis, M. L. P. Reddy, Lysosome-targeting luminescent lanthanide complexes: From molecular design to bioimaging. *Dalton Trans.* **51**, 7748–7762 (2022).
29. W. Zhang *et al.*, A lysosome-targeting nanosensor for simultaneous fluorometric imaging of intracellular pH values and temperature. *Mikrochim. Acta* **185**, 533 (2018).
30. B. del Rosal *et al.*, In vivo contactless brain nanothermometry. *Adv. Funct. Mater.* **28**, 1806088 (2018).
31. A. Gupta *et al.*, Up-conversion hybrid nanomaterials for light- and heat-driven applications. *Prog. Mater. Sci.* **121**, 100838 (2021).
32. Z. Shi *et al.*, Dual functional $NaYF_4$:Yb^{3+}, Er^{3+}@$NaYF_4$:Yb^{3+}, Nd^{3+} core-shell nanoparticles for cell temperature sensing and imaging. *Nanotechnology* **29**, 094001 (2018).
33. X. Qiu *et al.*, Ratiometric upconversion nanothermometry with dual emission at the same wavelength decoded via a time-resolved technique. *Nat. Commun.* **11**, 4 (2020).
34. Y. He *et al.*, A combinational chemo-immune therapy using an enzyme-sensitive nanoplatform for dual-drug delivery to specific sites by cascade targeting. *Sci. Adv.* **7**, eaba0776 (2021).
35. L. Zhang *et al.*, Optimizing the polymer cloak for upconverting nanoparticles: An evaluation of bioactivity and optical performance. *ACS Appl. Mater. Interfaces* **13**, 16142–16154 (2021).
36. M. Maddahfar *et al.*, Stable and highly efficient antibody-nanoparticles conjugation. *Bioconjug. Chem.* **32**, 1146–1155 (2021).
37. J. Adler, I. Parmryd, Quantifying colocalization by correlation: The Pearson correlation coefficient is superior to the Mander's overlap coefficient. *Cytometry A* **77**, 733–742 (2010).
38. Y. Takei *et al.*, A nanoparticle-based ratiometric and self-calibrated fluorescent thermometer for single living cells. *ACS Nano* **8**, 198–206 (2014).
39. A. F. Slater, A. Cerami, Inhibition by chloroquine of a novel haem polymerase enzyme activity in malaria trophozoites. *Nature* **355**, 167–169 (1992).
40. C. A. Homewood, D. C. Warhurst, W. Peters, V. C. Baggaley, Lysosomes, pH and the anti-malarial action of chloroquine. *Nature* **235**, 50–52 (1972).
41. A. C. Cutró, G. G. Montich, O. A. Roveri, Effect of carbonylcyanide-4-(trifluoromethoxy)phenylhydrazone (FCCP) on the interaction of 1-anilino-8-naphthalene sulfonate (ANS) with phosphatidylcholine liposomes. *J. Bioenerg. Biomembr.* **46**, 119–125 (2014).
42. S. Kiyonaka *et al.*, Genetically encoded fluorescent thermosensors visualize subcellular thermoregulation in living cells. *Nat. Methods* **10**, 1232–1238 (2013).
43. M. Homma, Y. Takei, A. Murata, T. Inoue, S. Takeoka, A ratiometric fluorescent molecular probe for visualization of mitochondrial temperature in living cells. *Chem. Commun. (Camb.)* **51**, 6194–6197 (2015).

44. D. Chrétien *et al.*, Mitochondria are physiologically maintained at close to 50 °C. *PLoS Biol.* **16**, e2003992 (2018).
45. J. Qiao *et al.*, Simultaneous monitoring of mitochondrial temperature and ATP fluctuation using fluorescent probes in living cells. *Anal. Chem.* **90**, 12553–12558 (2018).
46. K. Okabe *et al.*, Intracellular temperature mapping with a fluorescent polymeric thermometer and fluorescence lifetime imaging microscopy. *Nat. Commun.* **3**, 705 (2012).
47. T. Hayashi, N. Fukuda, S. Uchiyama, N. Inada, A cell-permeable fluorescent polymeric thermometer for intracellular temperature mapping in mammalian cell lines. *PloS one* **10**, e0117677 (2015).
48. R. Tanimoto *et al.*, Detection of temperature difference in neuronal cells. *Sci. Rep.* **6**, 22071 (2016).
49. G. Baffou, H. Rigneault, D. Marguet, L. Jullien, A critique of methods for temperature imaging in single cells. *Nat. Methods* **11**, 899–901 (2014).
50. D. Macherel, F. Haraux, H. Guillou, O. Bourgeois, The conundrum of hot mitochondria. *Biochim. Biophys. Acta Bioenerg.* **1862**, 148348 (2021).
51. G. Baffou, H. Rigneault, D. Marguet, L. Jullien, Reply to: "Validating subcellular thermal changes revealed by fluorescent thermosensors" and "The 10(5) gap issue between calculation and measurement in single-cell thermometry". *Nat. Methods* **12**, 803 (2015).
52. C. Wang *et al.*, Dynamic tubulation of mitochondria drives mitochondrial network formation. *Cell Res.* **25**, 1108–1120 (2015).
53. N. Lane, Hot mitochondria? *PLoS Biol.* **16**, e2005113 (2018).
54. J. Zielonka *et al.*, Mitochondria-targeted triphenylphosphonium-based compounds: Syntheses, mechanisms of action, and therapeutic and diagnostic applications. *Chem. Rev.* **117**, 10043–10120 (2017).
55. D. F. Rolfe, G. C. Brown, Cellular energy utilization and molecular origin of standard metabolic rate in mammals. *Physiol. Rev.* **77**, 731–758 (1997).
56. C. Riedel *et al.*, The heat released during catalytic turnover enhances the diffusion of an enzyme. *Nature* **517**, 227–230 (2015).
57. K. Richter, M. Haslbeck, J. Buchner, The heat shock response: Life on the verge of death. *Mol. Cell* **40**, 253–266 (2010).
58. J. Qin *et al.*, ER-mitochondria contacts promote mtDNA nucleoids active transportation via mitochondrial dynamic tubulation. *Nat. Commun.* **11**, 4471 (2020).
59. H. Hao *et al.*, Golgi-associated microtubules are fast cargo tracks and required for persistent cell migration. *EMBO Rep.* **21**, e48385 (2020).
60. Y. Liu *et al.*, Stratified disk microrobots with dynamic maneuverability and proton-activatable luminescence for *in vivo* imaging. *ACS Nano* **15**, 19924–19937 (2021).
61. C. Chen *et al.*, Multi-photon near-infrared emission saturation nanoscopy using upconversion nanoparticles. *Nat. Commun.* **9**, 3290 (2018).
62. J. Zhou, A. I. Chizhik, S. Chu, D. Jin, Single-particle spectroscopy for functional nanomaterials. *Nature* **579**, 41–50 (2020).
63. X. Yang *et al.*, Mitochondrial dynamics quantitatively revealed by STED nanoscopy with an enhanced squaraine variant probe. *Nat. Commun.* **11**, 3699 (2020).
64. Q. P. Su *et al.*, Superresolution imaging reveals spatiotemporal propagation of human replication foci mediated by CTCF-organized chromatin structures. *Proc. Natl. Acad. Sci. U.S.A.* **117**, 15036–15046 (2020).
65. Y. Chen, Q. P. Su, Y. Sun, L. Yu, Visualizing autophagic lysosome reformation in cells using in vitro reconstitution systems. *Curr. Protocols Cell Biol.* **78**, 11.24.11–11.24.15 (2018).
66. X. Zhu *et al.*, Temperature-feedback upconversion nanocomposite for accurate photothermal therapy at facile temperature. *Nat. Commun.* **7**, 10437 (2016).
67. B. Liu *et al.*, Upconversion nonlinear structured illumination microscopy. *Nano Lett.* **20**, 4775–4781 (2020).
68. Q. P. Su, L. A. Ju, Biophysical nanotools for single-molecule dynamics. *Biophys. Rev.* **10**, 1349–1357 (2018).
69. D. J. Chung *et al.*, Mitochondria, temperature, and the pace of life. *Integr. Comp. Biol.* **58**, 578–590 (2018).
70. M. Wang, G. Abbineni, A. Clevenger, C. Mao, S. Xu, Upconversion nanoparticles: Synthesis, surface modification and biological applications. *Nanomedicine (Lond.)* **7**, 710–729 (2011).
71. H. T. T. Duong *et al.*, Systematic investigation of functional ligands for colloidal stable upconversion nanoparticles. *RSC Advances* **8**, 4842–4849 (2018).
72. C. D. S. Brites, A. Millán, L. D. Carlos, "Lanthanides in luminescent thermometry" in *Handbook on the Physics and Chemistry of Rare Earths*, B. Jean-Claude, P. K. Vitalij, Ed. (Elsevier, 2016), vol. 49, chap. 281, pp. 339–427.